JACS Au
AN OPEN ACCESS JOURNAL OF THE AMERICAN CHEMICAL SOCIETY

pubs.acs.org/jacsau

Article

# Origin of Metal Cluster Tuning Enzyme Activity at the Bio-Nano Interface

Yufei Cao, Yida Qiao, Shitong Cui, and Jun Ge*

Cite This: *JACS Au* 2022, 2, 961−971

Read Online

ACCESS | Metrics & More | Article Recommendations | Supporting Information

**ABSTRACT:** Detailed understanding of how the bio-nano interface orchestrates the function of both biological components and nanomaterials remains ambiguous. Here, through a combination of experiments and molecular dynamics simulations, we investigated how the interface between *Candida Antarctic* lipase B and palladium (Pd) nanoparticles (NPs) tunes the structure, dynamics, and catalysis of the enzyme. Our simulations show that the metal binding to protein is a shape matching behavior and there is a transition from saturated binding to unsaturated binding along with the increase in the size of metal NPs. When we engineered the interface with the polymer, not only did the critical size of saturated binding of metal NPs become larger, but also the disturbance of the metal NPs to the enzyme function was reduced. In addition, we found that an enzyme−metal interface engineered with the polymer can boost bio-metal cascade reactions via substrate channeling. Understanding and control of the bio-nano interface at the molecular level enable us to rationally design bio-nanocomposites with prospective properties.

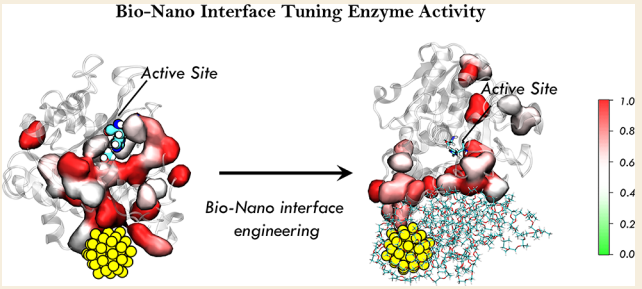


**KEYWORDS:** *metal cluster, enzyme, bio-nano interface, polymer engineering, substrate channeling*

## INTRODUCTION

Bio-nanomaterials with a well-defined composition, structure, surface chemistry, and functionalization can be sophisticatedly synthesized, with wide applications in biocatalysis,[1−3] bioimaging,[4] biosensing,[5] drug delivery,[6] and therapeutics for diagnosis and treatment of human diseases.[7,8] In these application scenarios, one important issue is that the physicochemical interactions, kinetics, and thermodynamics intricately affect the formation of bio-nano interfaces,[9] in processes including self-assembly of biomolecules with organic[2] and inorganic materials,[1,10] formation of protein coronas,[11] particle wrapping,[12] intracellular uptake of nanoparticles (NPs),[13] and nanomaterials manipulating cellular function.[14] The formed bio-nano interface mediates the properties and functions of both biomolecules and nanomaterials, such as protein conformation,[11] enzyme activity,[15−17] fate, transport, and toxicity of nanomaterials in living systems.[11,18] Thus, the in-depth understanding and precise manipulating of the bio-nano interface are the key for rationally designing novel hybrid materials with prospective properties and safe use of nanomaterials.[9]

For biocatalysis, the enzyme-nano interface is a key factor that needs to be considered, not only in enzyme immobilization with various nanoscaffolds[19−21] but also in the enzyme−metal NP complexes.[16,22] However, the mechanistic understanding of how nanomaterials affect the enzyme structure and function is still in its infancy. Several recent studies have aimed at providing some mechanisms of interaction-encoded enzyme property change.[23,24] To understand the physicochemical behavior of the bio-nano interface, a versatile but not complicated and easily controlled model system is needed. Our recent work on enzyme−metal complex shows the possibility.[16] In our work, single lipase−polymer conjugates as confined nanoreactors were utilized for the in situ generation of metal clusters, which shows the advantage in the controllable synthesis of clusters with different sizes from 2.5 to 0.8 nm. It is worth mentioning that the advantage of this synthetic method came from polymer engineering. It indicates that the polymer stabilized the enzyme−metal interface but the mechanism understanding was lacking.

In this work, relying on the advantage of the synthetic method we developed before, we illustrated how the interaction on bio-metal interface stabilizes metal clusters and tunes enzyme activity. We found that the metal binding to protein is a shape matching behavior and a transition from saturated binding to unsaturated binding along with the increasing size of metal NPs exists. Interestingly, polymer

Received: February 5, 2022
Revised: March 29, 2022
Accepted: March 30, 2022
Published: April 11, 2022





https://doi.org/10.1021/jacsau.2c00077
*JACS Au* 2022, 2, 961−971

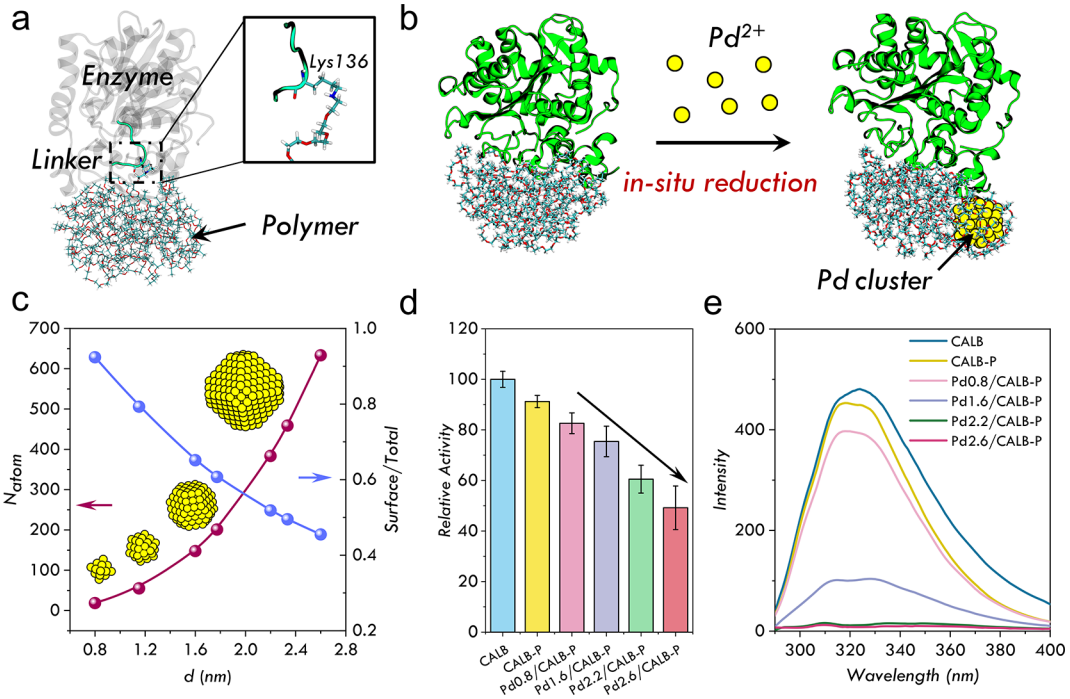


**Figure 1.** Size-dependent activity of enzyme−metal nanohybrids. (a) Structure of CALB−polymer conjugates. Lys136 is the linker between the CALB molecule and the F127 polymer. (b) In situ reduction of $Pd^{2+}$ to Pd NPs within the confinement of the enzyme−polymer nanoreactor. (c) Number of atoms of Pd NPs ($N_{atom}$) and the fraction of surface atoms of Pd NPs as a function of the diameter $d$ of Pd NPs. The geometries of four Pd NPs with different sizes (Pd19, Pd55, Pd201, and Pd459) were given. (d) Enzyme activities of CALB, CALB-P conjugates, and $x$Pd/CALB-P nanohybrids ($x$ = 0.8, 1.6, 2.2, and 2.5). (e) Fluorescence spectra of CALB, CALB-P conjugates, and $x$Pd/CALB-P nanohybrids ($x$ = 0.8, 1.6, 2.2, and 2.5). The same protein concentration was used for all samples.

engineering of the interface can not only make the critical size of saturated binding of metal NPs larger but also reduce the disturbance of the metal NPs to the enzyme function. Our results also showed that polymer engineering can boost the enzyme−metal cascade reaction through substrate channeling. We believe that our work can provide some principles for rational bio-nano interface engineering.

## RESULTS AND DISCUSSION

### Size-Dependent Activity of Enzyme−Metal Nanohybrids

First, we synthesized enzyme−polymer conjugates through covalently linking *Candida Antarctic* lipase B (CALB) with an amphiphilic poly(ethylene oxide)−poly(propylene oxide) block copolymer named Pluronic F-127 via the Schiff base reaction (Figure S1, detailed in the Supporting Information) according to our previous work.[16] Each conjugate (CALB-P) contained one polymer chain attached to one CALB molecule (Figure 1a). Our previous analysis showed that Lys136 is the most possible bonding site of the polymer.[16] In the following simulation and analysis, Lys136 was considered as a linker between the enzyme molecule and polymer chain. $Pd^{2+}$ was reduced within the confinement of the enzyme−polymer nanoreactor, generating size-controllable Pd NPs (Figure 1b). Using different concentrations of $Pd(OAc)_2$, the size of Pd NPs was tuned from 2.5 to 0.8 nm (2.5, 2.2, 1.6, and 0.8 nm), denoted as 2.5Pd/CALB-P, 2.2Pd/CALB-P, 1.6Pd/CALB-P, and 0.8Pd/CALB-P, respectively (Figure 1c and Table S1). This size change not only tunes the activity of Pd NPs but also regulates the activity of CALB. As shown in Figure 1d, the polymer attachment did not obviously affect the CALB activity, but the large Pd NPs significantly inhibited the enzyme activity. 2.5Pd/CALB-P only reserved half activity of the original CALB, while 0.8Pd/CALB reserved more than 80% activity of CALB. It indicates that the small Pd NPs may have less influence on the structure and essential motions related to enzyme catalysis. The results of fluorescence spectra showed that the influence of large Pd NPs on the tertiary structure of CALB (Figure 1e) was arresting, and it may be the origin of activity loss of the enzyme. In the following section, molecular dynamics (MD) simulations will be employed to investigate how Pd NPs with different sizes were stabilized in the confinement of CALB-P and how they affected the structure and activity of CALB.

### Bio-metal Interface between CALB and Pd NPs

Although a protein is widely utilized as a carrier for the synthesis of metal NPs,[15,25−28] the mechanism of interaction between metal NPs and the protein is lacking. We began with the study of binding behavior between CALB and Pd NPs with different sizes. It serves as a comparison with the case of Pd NPs/CALB-P and helps us deeply understand the role of the polymer in the formation of the bio-nano interface. We selected truncated octahedron-shaped Pd NPs with four sizes including Pd19, Pd55, Pd201, and Pd459 in our simulations (Tables S2 and S3). The diameter of these NPs was 0.8 nm, 1.2 nm, 1.8 nm, and 2.3 nm, respectively, which reproduces the size of Pd NPs in the synthesized nanohybrids (Figure 1d). To find the most stable complex of enzyme−metal NPs, shape-matched docking[29] and MD simulations was conducted in combination (see Materials and Methods and Figures S2−S7). In short, we generated multiple candidates of binding structures through rigid docking and then further optimized the structures through MD simulation to find the most stable


https://doi.org/10.1021/jacsau.2c00077
JACS Au 2022, 2, 961−971

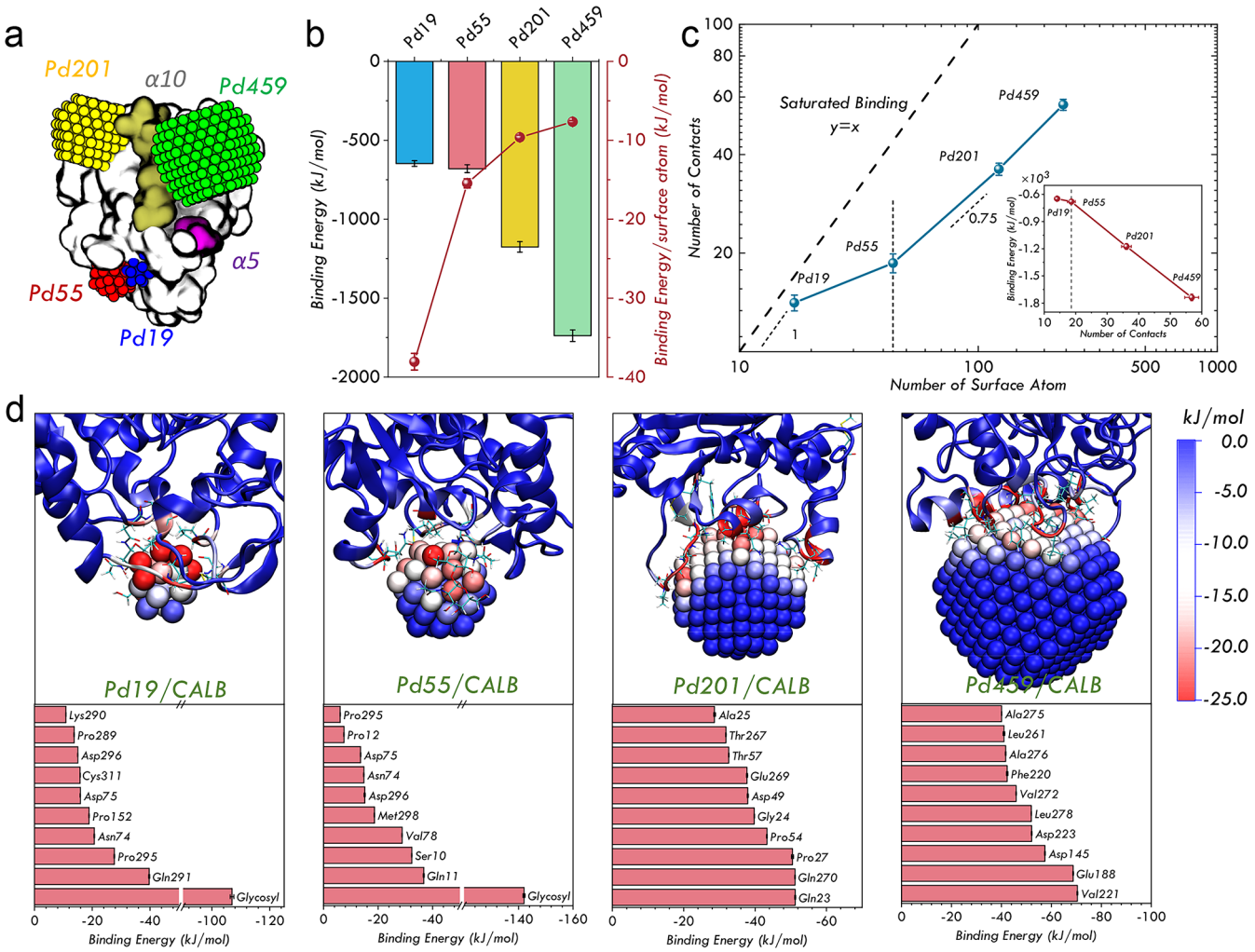


**Figure 2.** Binding behavior between CALB and Pd NPs with different sizes. (a) Optimal binding structures of Pd NPs with four sizes obtained through docking and MD simulations. Two alpha helixes near the active site named $\alpha$5 and $\alpha$10 were marked. (b) Binding energy and average interaction felt by the surface atoms (binding energy/surface atom) of Pd NPs with different sizes. (c) The number of contacts of Pd NPs with protein ($N_C$) is plotted vs the number of surface atoms of Pd NPs ($N_S$). Inset: binding energy of Pd NPs vs the number of contacts. (d) Binding energy distribution of Pd19/CALB, Pd55/CALB, Pd201/CALB, and Pd459/CALB (the last 0.5 $\mu$s long trajectories were used for calculations). The 10 residues that contribute the most to the binding energy were listed.

binding states. The final binding structures for all Pd NPs were obtained by microsecond long MD simulations. This method can serve as a standard procedure for studying the binding of proteins with metal NPs (Figures S3 and S4). Our simulation results indicate that the binding of metal NPs on the surface of the protein is a shape matching behavior, which is consistent with our prediction (Figure S2). It means that the metal NPs tend to bind with a shape-matched surface region of the protein. A nonspecific van der Waals interaction drives metal NPs to find a shape matching region on the surface of the protein that has more contacts with metal NPs. It is worth noting that a shape matching glycosylation on the protein surface can provide significantly more stabilization for small metal NPs (Figure S5). Hence, surface modification of the protein could be beneficial to metal NP binding. As shown in Figures 2a, S6, and S7, we finally obtained the optimal binding structure of Pd NPs with four sizes. The binding sites of Pd19 and Pd55 were adjacent because of the existence of the glycosyl group. The binding energy obtained from MD simulations showed that larger Pd NPs had more interaction with protein, but the average interaction felt by the surface atoms gradually decreased (Figure 2b). Interestingly, we noticed that Pd19 and Pd55 had almost the same binding energy with protein, but the average interaction felt by the surface atoms dropped steeply. It indicates that there is a binding mode transition from Pd19 to Pd55. To investigate this transition, we analyzed the number of contacts of Pd NPs with protein. The number of contacts reflects the number of surface atoms interacting with protein. The binding energy had a good linear relationship with the number of contacts from Pd459 to Pd55 except for Pd19 (Figure 2c, inset). When we plotted the number of contacts of Pd NPs ($N_C$) with protein as a function of the number of surface atoms ($N_S$), we can observe that the binding mode transition is actually a transition from near-saturated binding to unsaturated binding. The saturated binding has the relationship $N_C = N_S$, while the unsaturated binding has a relationship $N_C = N_S^{\beta}$, where $\beta < 1$. The binding of Pd19 was located near the saturated binding region, and from Pd55 to Pd459, it was an unsaturated binding mode with an exponent $\beta = 0.75$. We can reasonably deduce that the binding behavior of metal NPs on the protein surface will transit from saturated binding to unsaturated binding with


https://doi.org/10.1021/jacsau.2c00077
JACS Au 2022, 2, 961−971

increasing size, and there exists a critical size. Only the metal NPs below the critical size can be effectively stabilized. The critical size depends on the surface structure of the protein. For CALB, the critical size is below 0.8 nm, and only extremely small Pd NPs such as Pd19 can be well stabilized by the surface of CALB. We decomposed the binding energy contributions in a per-residue basis through the molecular mechanics Poisson−Boltzmann surface area approach (Figure 2d, see Materials and Methods). For Pd19/CALB and Pd55/CALB, glycosyl had a remarkable contribution to the binding energy as it was a much larger group than protein residues. The top 10 residues with the highest binding energy contained many types of residues, and it confirmed the nonspecificity of Pd NP binding. With the increasing size of Pd NPs, the number of more strongly interacted residues increased, but the ratio of interacted Pd atoms decreased. From the binding energy distribution of Pd atoms (Figures 2d and S10b−e), we found that heterogeneity existed, and the corner and edge atoms had more binding contribution. It indicates that the corner and edge atoms of metal NPs are easier to bind with the protein surface. Hence, small metal NPs with more corner and edge atoms are more likely to be stabilized (Figure S10a). The size-dependent bio-nano interactions are key factors in imaging, drug delivery, diagnosis, and clinical therapeutic purposes.[30−32] It greatly affects the function and ultimate efficiency of nanomedicines. The critical size in Pd NP binding with the protein is speculated to exist in the bio-nano interaction between small NPs and protein. These conclusions can be utilized for rationally designing protein-nano complexes.

We then explored the influence of Pd NPs on the structure and dynamics of CALB. Compared with wild CALB, the structure of CALB in Pd NPs/CALB had obvious change except for Pd55/CALB (Figure S11). Some helixes near the Pd NP binding region uncoiled due to the interaction of Pd NPs. It indicates that metal binding may destroy the second structure of proteins. The root-mean-square deviation (RMSD) between the average structure of CALB in Pd NPs/CALB during equilibrium simulation and that of wild CALB is shown in Table 1. Pd55 had a minimum impact on the structure of CALB, and larger Pd NPs can obviously disturb the protein structure. To probe how Pd NP binding affects the dynamics of CALB, we calculated the Cα root-mean-square fluctuation (RMSF) for both Pd NPs/CALB and wild CALB states. Higher RMSF values correspond to greater flexibility during the simulation. Although the Cα RMSF profiles for Pd NPs/CALB and wild CALB states were similar, indicating similar dynamics, there were some discernible differences (Figures 3a and S12). In equilibrium simulations of wild CALB, the hydrophobic core of the enzyme was stable and showed limited fluctuations (Figure S14). Most of the RMSF variance was observed in the α5 region and the loop region near it and the α10 region. Nevertheless, these largely fluctuated regions were consistently restricted in Pd NPs/CALB. This phenomenon can also be observed in RMSD calculated as a function of the fraction Cα, core Cα RMSD superimposition, and average positional Cα deviations (Figures S13−S15). The conformational fluctuation of CALB was sometimes observed to be intensified, such as residues 25−32 of CALB in Pd201/CALB. In summary, the Pd NP binding makes the structure of CALB more rigid. In addition, this influence could be direct or indirect because Pd19 and Pd55 are not directly interacted with α5 and α10 regions. Principal component analysis (PCA) was carried out to further illustrate the change of conformation states of CALB after binding with Pd NPs. The average conformation of the CALB structure in Pd NPs/CALB was shifted relative to that of wild CALB (Figure 3b) when the dynamic configurations were projected onto the two principal vectors. We found that Pd55/CALB had the largest (69%) subspace overlap with wild CALB from the calculated dot product matrix (Figure S16). In contrast, Pd459/CALB had only a 53.8% subspace overlap. This conformation space shift may perturb the active site of CALB and cause activity loss. The binding sites of Pd NPs except for Pd459 were far from the active site (Figure S7). Therefore, remote regulation of Pd NPs to enzyme catalysis is likely to exist. To understand how conformational dynamics orchestrates allosteric regulation of catalysis, we calculated dynamic cross-correlation maps (DCCMs)[33,34] (Figure S17). DCCM results showed that Pd NP binding introduced some negative correlation between interacted residues and other noncontiguous residues, especially in Pd19/CALB and Pd459/CALB. The impact induced by Pd NPs was propagated into the active site through the dynamical network of protein. To investigate how the Pd perturbation is remotely felt by the active site of CALB, we then calculated the probability density distributions of side-chain torsion angles (PDSTAs).[35] A torsion angle analysis may be more sensitive than a contact analysis as more subtle changes can be captured.[36] Based on the change of the distributions of side-chain torsion angles, we can directly detect the subtle conformation change of the enzyme. We used the Jensen−Shannon (JS) divergence to measure the difference of torsion angle distributions across ensembles (see Materials and Methods). Dynamically "responsive" residues with apparently shifted distributions can be easily distinguished. Figure 3c shows the JS divergence of the probability density distributions of side-chain torsion angles of each amino acid residues of wild enzyme state and Pd binding states. It reflected the response of the whole protein to the perturbation of Pd NPs. We can find several responsive residues located both near and distal to the Pd NP binding site. Obviously, the active site felt the perturbation of Pd NPs. For instance, there were some responsive residues at the loop region where Asp187 is located. Both Ser105 and Asp187 of the catalytic triad were disturbed to various degrees. We summed the JS divergence of residues within 5 Å of the active site to show the perturbation of Pd NPs to the active site (Table 1). It indicates that Pd55 has the least impact on the active site while Pd459 has an arresting perturbation. By identifying responsive residues, we finally identified residue pathways connecting the Pd binding sites to the active site. There were two similar pathways in Pd19/CALB and Pd55/CALB mediating the allosteric communication between residues directly interacted with Pd NPs and the active site

**Table 1. RMSD between CALB in Pd NPs/CALB and That of Wild CALB and Summed JS Divergence of Residues within 5 Å of the Active Site[a]**

| System | RMSD (Å) | summed JS divergence |
|---|---|---|
| Pd19/CALB | 1.12 | 5.8 |
| Pd55/CALB | 0.86 | 4.2 |
| Pd201/CALB | 1.65 | 7.9 |
| Pd459/CALB | 1.68 | 15.4 |

[a]The higher value of JS divergence indicates a larger perturbation of Pd NPs to the active site of the enzyme.



https://doi.org/10.1021/jacsau.2c00077
JACS Au 2022, 2, 961−971

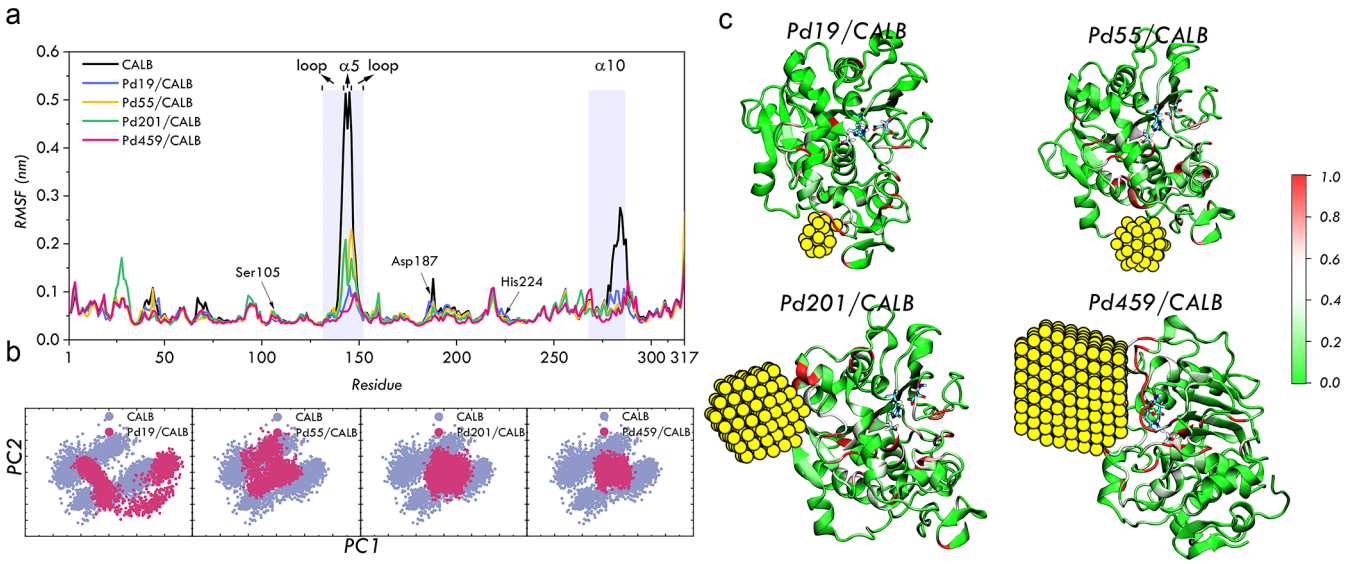


**Figure 3.** Influence of Pd NP binding on the structure and dynamics of CALB. (a) RMSF and the difference between CALB in the Pd NPs/CALB complex and wild CALB. The $\alpha$5 and $\alpha$10 regions and the catalytic triads Ser105, Asp187, and His224 were marked. (b) Dynamic conformations projected onto the vectors of two lowest-frequency principal components (PC1 and PC2). (c) Visualization of JS divergence of the probability distribution of side-chain torsion angles between Pd NPs/CALB and wild CALB. From green to red, the JS divergence gradually increases. The catalytic triads Ser105, Asp187, and His224 were shown.

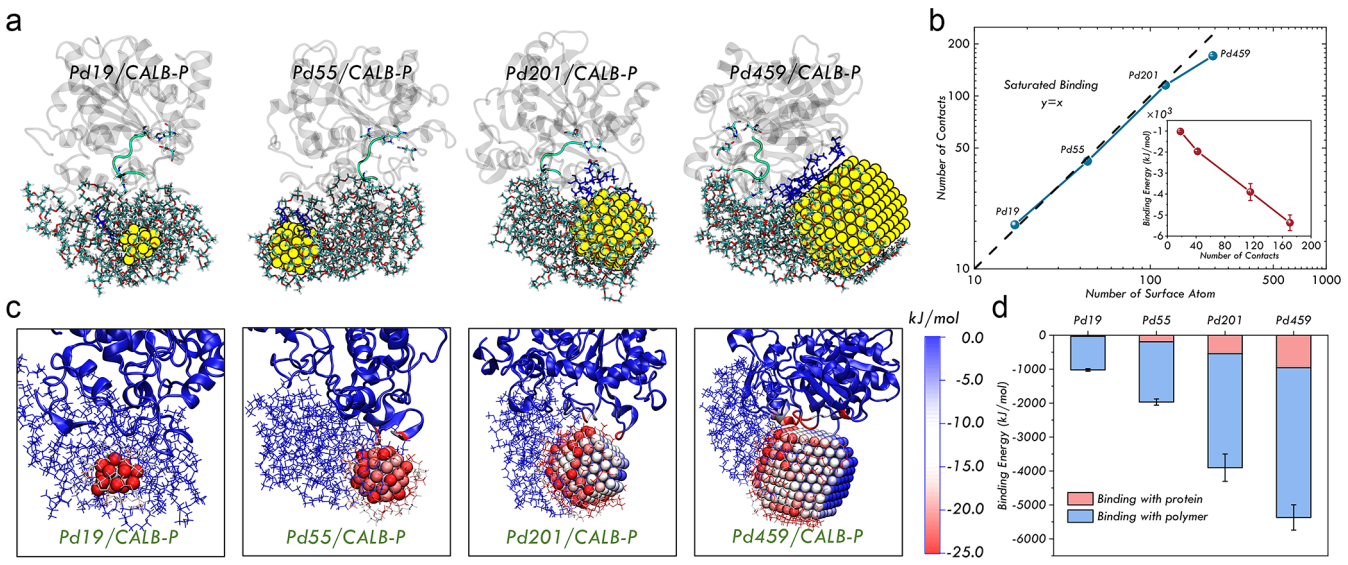


**Figure 4.** Binding behavior between CALB-P and Pd NPs with different sizes. (a) Optimal binding structures of Pd NPs with four sizes obtained through MD simulation. The amino acid residues of the enzyme interacted with Pd NPs were shown with blue color and the catalytic triad was also shown. (b) The number of contacts of Pd NPs with protein ($N_C$) is plotted vs the number of surface atoms of Pd NPs ($N_S$). Inset: binding energy of Pd NPs vs the number of contacts. (c) Binding energy distribution of Pd19/CALB-P, Pd55/CALB-P, Pd201/CALB-P, and Pd459/CALB-P. (d) Proportion of binding energy contributed by the protein and polymer in Pd19/CALB-P, Pd55/CALB-P, Pd201/CALB-P, and Pd459/CALB-P.

(Figures S18–S23). One pathway was identified in Pd201/CALB (Figures S24 and S25), and no pathway was identified in Pd459/CALB since Pd459 directly interacted near the active site (Figures S26 and S27). Taking the results of various analyses together, we can conclude that Pd55 has the least influence on the conformation of CALB, followed by Pd19, Pd201, and Pd459. Large metal NPs cause severe damage to the protein structure. Interestingly, a smaller size is not always better, although Pd19 can be better stabilized by CALB.

## Bio-metal Interface between CALB-P and Pd NPs

According to the results of our experiments, CALB-P has an obvious advantage in controllably synthesizing Pd NPs.[16] We then comprehensively investigated the origin of the advantage of CALB-P by MD simulations. We built the model of CALB-P and obtained the equilibrium state of it through enhanced conformational sampling, followed by 1 $\mu$s long MD simulation (see Materials and Methods, Figures 1a and S28–S30). In water, CALB and polymer were loosely complexed, and only ~10% of the CALB surface was covered by the polymer, which is different from the structure in organic solvent.[2,16] The polymer did not induce perceivable structure change to CALB (Figure S31). The RMSF variance in the $\alpha$5 region and the loop region near it and in the $\alpha$10 region were also reduced (Figures S32 and S33). We speculated that the


https://doi.org/10.1021/jacsau.2c00077
JACS Au 2022, 2, 961–971

dynamics of these regions could be restrained when a partner interacts with CALB. The restraining is not distinctly harmful to the activity of CALB as CALB-P reserved ∼90% activity of CALB in our experiments (Figure 1d). Analysis of DCCMs and PDSTA showed the negligible influence of polymer on dynamic networks of CALB (Figure S34). It is consistent with the experimental results. We then obtained the optimal complex structure of Pd NPs/CALB-P through a longtime MD simulation with different starting geometries (see Materials and Methods, Figures S35−S40). Figure 4a shows the structures of Pd19/CALB-P, Pd55/CALB-P, Pd201/CALB-P, and Pd459/CALB-P. The binding positions of Pd NPs with CALB-P varied from each other. The Pd NPs interacted with both the protein and the polymer, and the binding region with protein increased with larger Pd NPs. The most surface of Pd NPs was covered by the polymer chain. With the Pd NPs becoming larger, it was more difficult to be enwound by the polymer just as Pd459. There is an enthalpy−entropy competition in polymer coating behavior. Although the coating behavior is enthalpy favored, it will be inhibited when the entropy loss of polymer is insufferable. Hence, large Pd NPs can only be partially coated by the polymer. Interestingly, the pattern of polymer absorbed on the surface of Pd201 and Pd459 had a folding form like the parallel arrangement of polymers in the lamellae (Figure S41). The binding energy between Pd NPs and CALB-P increased with the increasing size of Pd NPs, and no sharp drop of the average interaction was felt by the surface atoms (Figure S44). The binding energy had a good linear relationship with the number of contacts (Figure 4b, inset). Hence, it elucidates that no transition happens, and it is verified in Figure 4b. Pd19, Pd55, and Pd201 were located at the saturated binding region, and Pd459 was nearly saturatedly bound. CALB-P can provide a larger critical size of saturated binding of metal NPs (>1.8 nm). This explains why the Pd NPs can be more controllably synthesized in CALB-P. Figure 4c shows the binding energy distribution in each case. With the increasing size of Pd NPs, more binding energy was contributed by the protein (Figure 4d), while the polymer was always the major contributor. The flexibility of the polymer enables it to bind with metal NPs abundantly and tunes the critical size of saturated binding.

Compared with Pd NPs/CALB, the structure of CALB in Pd NPs/CALB-P was less affected by Pd NPs (Figure S45), and no obvious helix uncoiling happened (RMSD in Table 2). The results of RMSF of Pd NPs/CALB-P were similar to that of CALB-P (Figure 5a), and conformational fluctuation in the $\alpha$5 region and the loop region near it and in the $\alpha$10 region was also reduced (Figures S46−S48). PCA further illustrates that the change of conformation states of CALB in the Pd NPs/CALB-P complex shows a conspicuous size-dependent effect. The larger the Pd NPs were, the larger the shift of conformation space would be induced by Pd NPs (Figure 5b). The subspace overlap of conformation with wild CALB decreased with the increasing size of Pd NPs from 78.4 to 62.9% (Figure S49). DCCM results also showed that the disturbance of Pd NPs in the Pd NPs/CALB-P complex to the dynamic networks of CALB was alleviated compared with that of Pd NPs/CALB (Figure S50). The DCCMs of Pd19/CALB-P and Pd55/CALB-P were nearly the same as that of CALB, while some negative correlations were introduced in the DCCMs of Pd201/CALB-P and Pd459/CALB-P. The difference of the PDSTA of each residue from wild state to Pd binding states in Pd NPs/CALB-P further demonstrated the protection function of the polymer and pathways of communication between residues directly interacted with Pd NPs and the active site (Figure 5c). The active site of CALB in Pd19/CALB-P and Pd55/CALB-P was slightly affected except for a small region near Asp187. Although many large shifted probability density distributions of angles existed in Pd201/CALB-P and Pd459/CALB-P, the degree of influence was less than Pd201/CALB and Pd459/CALB (summed JS divergence in Table 2). The pathway of propagation of perturbation was also identified in Pd55/CALB-P, Pd201/CALB-P, and Pd459/CALB-P (Figures S52−S57). All these results show the advantages of polymer engineering in both stabilization of metal NPs and protection of protein function. Polymers play the role of a mediator in the bio-nano interaction at the interface.

**Table 2. RMSD between CALB in Pd NPs/CALB-P and That of Wild CALB and Summed JS Divergence of Residues within 5 Å of the Active Site**

| system | RMSD (Å) | summed JS divergence |
|---|---|---|
| Pd19/CALB-P | 0.71 | 2.1 |
| Pd55/CALB-P | 0.82 | 3.8 |
| Pd201/CALB-P | 1.01 | 6.8 |
| Pd459/CALB-P | 1.24 | 12.8 |

## Substrate Channeling in Pd NPs/CALB-P

In nature, electrostatic guidance is an effective manner to control the diffusion of charged reaction intermediates between the catalytic active sites of two enzymes; this process is known as substrate channeling.[37] This natural phenomenon has been applied to artificial reaction cascades.[19,38] A special channel which can facilitate diffusion of the intermediates is the key to substrate channeling. Inspired from it, we envisioned that the polymer on the enzyme−metal interface of Pd NPs/CALB-P could serve as a bridge to facilitate restricted diffusion of a hydrophobic intermediate between the catalytic sites of enzyme and Pd NPs (Figure 6a). We can find that the polymer linked the enzyme and Pd NPs as a continuous medium in the complex of Pd NPs/CALB-P (Figure 4a). We guess that before diffusing to the bath, the intermediate products catalyzed by the enzyme may diffuse directly from the active site of the enzyme to Pd NPs through a polymer medium. The cascade reaction can be boosted by this substrate channeling phenomenon. To verify this hypothesis, we designed a model cascade reaction catalyzed by 0.8Pd/CALB-P in water. The cascade consisting of the ester hydrolysis reaction catalyzed by CALB and the Suzuki reaction catalyzed by Pd NPs can take place in two ways (Figure 6b). We assumed that the hydrophobic intermediate 2 or 3 can diffuse directly between the enzyme and Pd NPs. We synthesized the Pd NPs on the bovine serum albumin-polymer conjugates (BSA-P) with the same size and activity (Figure S58) and used the cascade reaction catalyzed by Pd NPs/BSA-P and CALB-P as a reference reaction. Figure 6c showed the catalytic performance of 0.8Pd/CALB-P and the performance of the combination of 0.8Pd/BSA-P and CALB-P. The cascade reaction of 0.8Pd/CALB-P was obviously boosted, which proved our hypothesis. We also performed MD simulations to further prove that the reaction intermediates can directly diffuse between the enzyme and Pd NPs. The results showed that the intermediate 2 can be transferred from the active site of CALB to the surface of Pd


https://doi.org/10.1021/jacsau.2c00077
JACS Au 2022, 2, 961−971

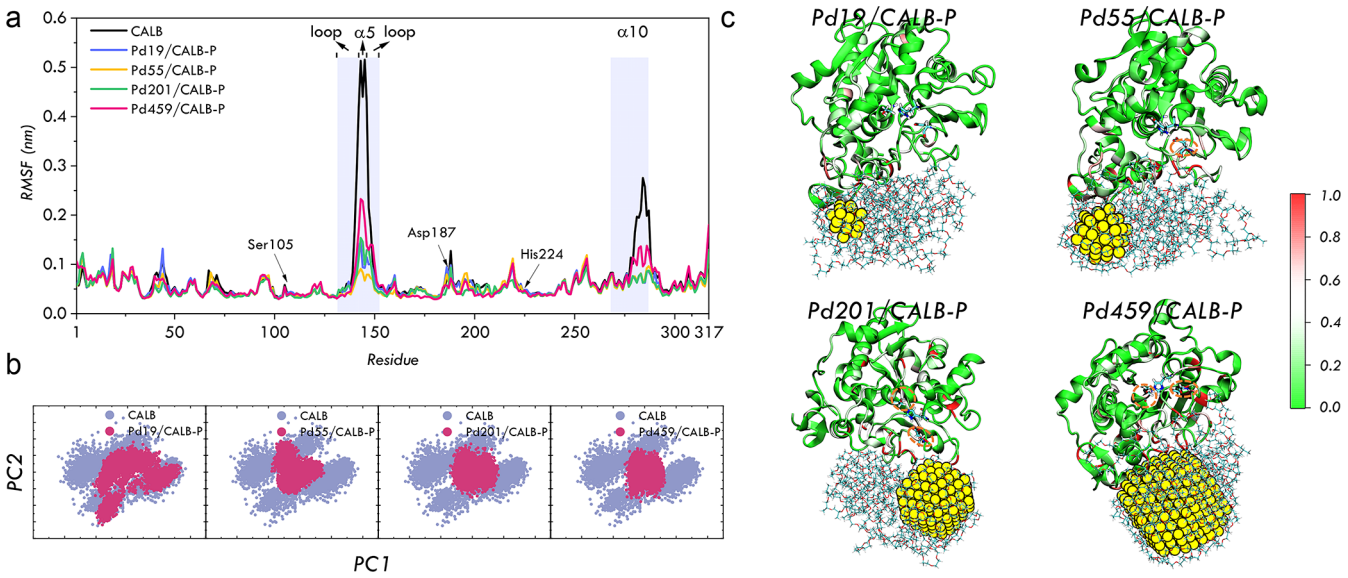


**Figure 5.** Influence of Pd NP binding on the structure and dynamics of CALB in Pd NPs/CALB-P. (a) RMSF and the difference between CALB in the Pd NPs/CALB-P complex and wild CALB. The $\alpha$5 and $\alpha$10 regions and the catalytic triads Ser105, Asp187, and His224 were marked. (b) Dynamic conformations projected onto the vectors of two lowest-frequency principal components (PC1 and PC2). (c) Visualization of JS divergence of the probability distribution of side-chain torsion angles between Pd NPs/CALB-P and wild CALB. From green to red, the JS divergence gradually increases. The catalytic triads Ser105, Asp187, and His224 were shown.

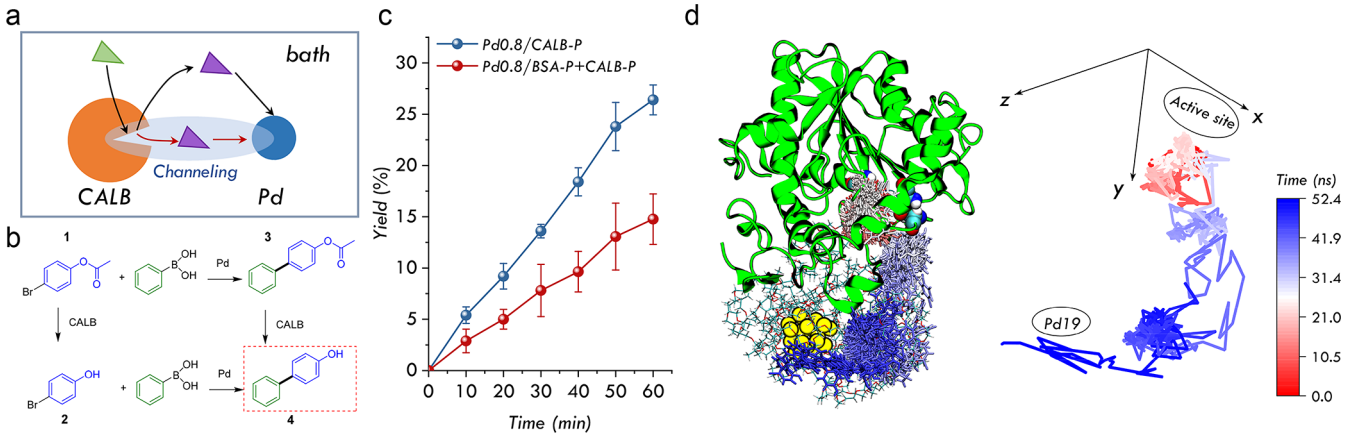


**Figure 6.** Substrate channeling in the bio-metal cascade reaction catalyzed by 0.8Pd/CALB-P. (a) Schematic diagram of the possible substrate channeling effect in 0.8Pd/CALB-P. (b) Bio-metal cascade reaction catalyzed by 0.8Pd/CALB-P. (c) Catalytic performance of 0.8Pd/CALB-P at 50 °C and performance of the combination of 0.8Pd/BSA-P and CALB-P in the cascade reaction. (d) Diffusion of intermediate products (intermediate 2) from the active site to Pd19 in MD simulation.

NPs, which was mediated by the polymer. Our studies demonstrated that polymer engineering on the enzyme−metal interface can not only protect enzymes but also boost bio-metal cascade reactions through substrate channeling.

## CONCLUSIONS

In summary, we investigated the mechanism of enzyme−metal NP interface tuning enzyme activity and shed some light on the principles of bio-nano interface engineering. We found that the metal NP binding is a shape matching behavior, and the binding sites varied between different sizes of metal NPs. With the increasing size of metal NPs, the binding behavior of metal NPs on the protein surface transits from saturated binding to unsaturated binding, and a critical size exists. In addition, metal NPs obviously disturb the structure, dynamics, and catalysis of the enzyme. The tight binding of metal NPs causes the loss of protein function, and the bio-metal interface should be engineered to protect the protein function. We showed how the polymer engineering of the interface makes the critical size of saturated binding of metal NPs larger and reduces the disturbance of the metal NPs to enzyme function. The mechanism of interaction on the enzyme−metal interface and how the structure and activity of the enzyme are influenced would enable us to rationally design the bio-nano interface at the molecular level.

## MATERIALS AND METHODS

### Shape-Matched Docking between the Protein and Metal NPs

The interaction between Pd NPs and protein comes from the van der Waals interaction, which is described through the Lennard-Jones (LJ) 12-6 potential (LJ potential). Based on our previous experience and LJ potential analysis (Figure S2), the interaction of Pd NPs is nonspecific. The key factor determining the interaction between Pd



https://doi.org/10.1021/jacsau.2c00077
JACS Au 2022, 2, 961−971

NPs and protein is the contact area between them. More contacts mean higher binding energy. Therefore, the problem of finding the most stable binding site of Pd NPs on the surface of the protein is converted to the problem of finding a shape-matched surface region of protein for Pd NP binding. Hence, docking is a suitable method for this problem. The PatchDock algorithm is inspired by object recognition and image segmentation techniques used in Computer Vision.[29] Given two molecules, PatchDock can divide two surfaces into patches according to the surface shape. These patches correspond to patterns that visually distinguish between puzzle pieces. Once the patches are identified, they can be superimposed using shape matching algorithms. This shape matching algorithm is appropriate for our problem. Using PatchDock and refinement of FireDock, we applied rigid-body docking for protein with Pd NPs of different sizes. Four truncated octahedral Pd NPs (Supporting Information Table 3) were selected. For each case, we obtained the top 100 highest scored complex structures. These structures were aligned into a single structure to see the position distribution of Pd NPs on the protein surface (Figure S4). Several possible binding sites were found, and the shape of the two surfaces was well matched. It indicates that PatchDock is very efficient. Generally, docking results showed that the possible binding sites of metal NPs decrease with increasing size. Although the top 100 highest scored docking results were selected, most of the positions were overlapped (Figure S4), and only several possible binding sites existed on the protein surface. Considering the flexibility of the Pd NPs in binding with protein, these docking structures were finally optimized through MD simulations, and the most stable binding structure was selected.

## MD Simulation of CALB and Complex of Pd NPs/CALB

The crystallographic structure of CALB (PDB ID: 1TCA)[39] was used as the starting geometry. PROPKA 3[40,41] was employed to assign the protonation states of titratable residues. In addition, the protonation states and side-chain orientations were also checked by visual inspection. All amino acid residues except for Asp134 were negatively charged, while alkaline Lys and Arg residues remained positively charged. His224, the only HIS residue, of the catalytic triad, was singly protonated at $N_\sigma$. The total charge of the protein was zero. There is an *N*-glycosylation site at Asn74, and the glycosylation was built by GLYCAM tools.[42] All crystal waters were retained. This processed structure was used as the initial structure for a subsequent MD simulation. All MD simulations of the complex of CALB and Pd NPs were conducted using GROMACS 2019.3,[43] along with the Amber ff14SB[44] force-field parameters and the reoptimized parameters for the $\omega$ torsional angle[45] for protein. The GLYCAM_06j-1[46] force field was used for glycans. The embedded atom model (EAM) was wildly used for metal simulation.[47] However, embedded atom potentials for metals are of an entirely different functional form and are very difficult to combine with force fields for polymers and biomolecules, which rely on harmonic energy expressions.[48] Heinz et al. presented 12-6 and 9-6 LJ parameters for several face-centered cubic metals (Ag, Al, Au, Cu, Ni, Pb, Pd, and Pt).[49] The performance is comparable to tight-binding and EAMs, and it has compatibility with widely used force fields, including AMBER, CHARMM, COMPASS, CVFF, OPLS-AA, and PCFF. It is embedded with some force fields such as the INTERFACE-CHARMM force field to simulate the properties of the bio-metal interface.[48,50] We embedded the 12-6 LJ potential parameters of Pd[49] into the Amber ff14SB force field to carry out our simulation. The initial geometries of CALB-Pd NPs were selected from docking results (Figure S3). We selected 9, 8, 4, and 5 possible complex structures from docking results of Pd19, Pd55, Pd201, and Pd459 as the initial geometries of simulations of Pd NPs/CALB. The Pd NPs/CALB complex was placed in a periodic cubic box of water molecules represented by the three-point charge TIP3P model, whose boundary is at least 15 Å from any atoms. The total system was energy-minimized by a succession of steepest descent and conjugate gradient methods. Thereafter, the solvent was equilibrated for 10 ns at a constant temperature (298.15 K) and pressure (1 bar) (*NPT*) by restraining the positions of the complex, followed by *NPT* equilibration for another 200 ns by restraining the positions of CALB (Pd NPs were free). Then, we calculated the binding energy between CALB and Pd NPs (Figure S4) through MMPBSA.[51−53] The structures with the highest binding affinity were selected for the following 1 $\mu$s long *NPT* simulation (298.15 K, 1 bar) without position restraints (2 $\mu$s for Pd19/CALB) (Figure S6). We used a V-rescale thermostat[54] and Parrinello−Rahman barostat[55] to maintain the temperature and pressure constant, respectively. The cutoff radius for neighbor searching and nonbonded interactions was taken to be 12 Å, and all bonds were constrained using the LINCS algorithm.[56]

## MD Simulation of CALB-P and Complex of Pd NPs/CALB-P

The polymer Pluronic F-127 ($PEO_{99}$−$PPO_{65}$−$PEO_{99}$) covalently bonds with CALB at Lys136. Parameters for the modified Lys136, PEO monomer, and PPO monomer were generated with the antechamber module of Amber18[57] using the general Amber force field (GAFF),[58] with partial charges set to fit the electrostatic potential generated with HF/6-31G(d) by RESP.[59] The model of CALB-P was generated through Ambertools[60] and VMD.[61] After modifying with polymer, the total charge of CALB-P is −1. The system was neutralized by adding one $Na^+$. The kinetics of entanglement of protein by Pluronic F-127 is beyond the capability of MD simulation because the polymer chain is long. Since sampling the thermodynamic equilibrium state of CALB-P is difficult, the following approach was employed to accelerate the process of finding the stable configuration of the protein−polymer conjugate. This approach was employed in some previous work.[2,16]

Step 1: The CALB−Pluronic conjugate was put in a cubic box. The initial structure under vacuum is given Figure S28, $V_b$. The CALB−Pluronic conjugate was simulated under vacuum for 20 ns, and the *NVT* ensemble (constant number of particles, temperature, and volume) was employed with the V-rescale thermostat (a constant temperature of 600 K). In this step, the heavy atom of CALB (except for H atom) was constrained at its initial coordinate to maintain the structure of CALB at high temperature.

Step 2: The obtained structure of the CALB−Pluronic conjugate under vacuum (Figure S28, $V_e$) was then embedded in water (Figure S28, $W_b$). The simulation at 600 K was performed to enhance the sampling of the CALB−Pluronic conjugate. The *NPT* ensemble (constant number of particles, temperature, and pressure) was applied. The temperature and pressure are coupled via the Vrescale algorithm and the isotropic Berendsen barostat (the reference pressure 1 bar). The simulation lasted for 200 ns with the CALB heavy atom constrained.

Step 3: After that, the position restraints of CALB were switched off. The final structure of the CALB−Pluronic conjugate (Figure S28 $W_e$) was obtained by simulation at 298.15 K for 1 $\mu$s (Figure S29).

Employing the above approach, we obtained similar equilibrium structures of the protein−polymer conjugate with different initial structures (Figure S30). It indicates that the approximate equilibrium state was obtained. Then, the obtained equilibrium structure was used for the simulation of Pd NPs/CALB-P. As our previous experimental study[16] indicates that Pd NPs were stabilized by both protein and polymer, we reasonably believe that the Pd NPs in the Pd NPs/CALB-P complex were located at the interface between the protein and the polymer. We selected eight starting positions of Pd NPs at the interface as the starting geometries of Pd NPs/CALB simulations. The simulation settings were the same as the simulation of Pd NPs/CALB. The complex in water was equilibrated for 10 ns at a constant temperature (298.15 K) and pressure (1 bar) (*NPT*) by restraining the positions of the complex, followed by *NPT* equilibration for another 200 ns by restraining the positions of CALB (Pd NPs and polymer were free). Then, we calculated the binding energy between CALB-P and Pd NPs (Figure S36). The structures with the highest binding affinity were selected for the following 1 $\mu$s long *NPT* simulation (298.15 K, 1 bar) without position restraints (Figures S37−S40).

## Analysis of MD Simulation Results

MMPBSA[51−53] was used for binding energy calculations and energy contribution of residues to the binding. The binding energy


https://doi.org/10.1021/jacsau.2c00077
JACS Au 2022, 2, 961−971

contribution of each residue was visualized by VMD.[61] The analysis of mobility and structural fluctuation of the simulation was realized by MDLovofit.[62] It allows the automatic identification of rigid and mobile regions of protein structures (Figures S13, S14, S46, and S47). DCCMs have been previously used to identify networks of coupled residues in enzymes. We calculated DCCMs using Bio3D.[63] PCA of the trajectories was carried out by using pyPcazip, a PCA-based toolkit for compression and analysis of molecular simulation data.[64] The distribution of side-chain torsion angle was calculated by python library MDTraj.[65] We examined side-chain torsion angles up to $\chi_2$. Glycine, alanine, and proline are excluded because they have no proper side-chain torsion angle. To quantitatively compare the influence of Pd NPs on the probability distribution of side-chain torsion angles, we used the JS divergence to measure the difference of two angle probability distributions. JS divergence is based on the Kullback–Leibler (KL) divergence, with some notable and useful differences, including that it is symmetric and it always has a finite value. For discrete probability distributions $P$ and $Q$ defined on the same probability space, $\chi$, the KL divergence from $Q$ to $P$ is defined as

$$\mathrm{KL}(P\|Q) = \sum_{x\in\chi} P(x)\log\left(\frac{P(x)}{Q(x)}\right)$$

and the JS divergence is defined as

$$\mathrm{JS}(P\|Q) = 1/2\mathrm{KL}\left(P\middle\|\frac{P+Q}{2}\right) + 1/2\mathrm{KL}\left(Q\middle\|\frac{P+Q}{2}\right)$$

Using the JS divergence, we visualized the change of probability distribution of side-chain torsion angles of each residue after Pd NP binding. When both $\chi_1$ and $\chi_2$ of a residue existed, the larger JS divergence was chosen.

## ■ ASSOCIATED CONTENT

### Supporting Information

The Supporting Information is available free of charge at https://pubs.acs.org/doi/10.1021/jacsau.2c00077.

Additional materials and methods, including the procedure of CALB-P/Pd NP synthesis, enzyme activity assays, and substrate channeling investigating; RMSD, RMSF, binding energy, and structural data of simulation; and results of DCCMs, PCA, and probability density distributions of side-chain torsion angles (PDF)

## ■ AUTHOR INFORMATION


### Corresponding Author

**Jun Ge** − *Key Lab for Industrial Biocatalysis, Ministry of Education, Department of Chemical Engineering, Tsinghua University, Beijing 100084, China; Institute of Biopharmaceutical and Health Engineering, Tsinghua Shenzhen International Graduate School, Shenzhen 518055, China; Institute of Biomedical Health Technology and Engineering, Shenzhen Bay Laboratory, Shenzhen 518107, China;* orcid.org/0000-0001-5503-8899; Email: junge@mail.tsinghua.edu.cn

### Authors

**Yufei Cao** − *Key Lab for Industrial Biocatalysis, Ministry of Education, Department of Chemical Engineering, Tsinghua University, Beijing 100084, China*

**Yida Qiao** − *Key Lab for Industrial Biocatalysis, Ministry of Education, Department of Chemical Engineering, Tsinghua University, Beijing 100084, China*

**Shitong Cui** − *Key Lab for Industrial Biocatalysis, Ministry of Education, Department of Chemical Engineering, Tsinghua University, Beijing 100084, China*

Complete contact information is available at: https://pubs.acs.org/10.1021/jacsau.2c00077


### Author Contributions

J.G. supervised the project. J.G. and Y.C. conceived the idea. Y.C. performed the experiments with technical help from Y.Q. and S.C. Y.C. performed the simulation and analysis. Y.C. and J.G. co-wrote the paper.

### Notes

The authors declare no competing financial interest.

## ■ ACKNOWLEDGMENTS

This work was supported by the National Key Research and Development Program of China (2021YFC2102800), the National Natural Science Foundation of China (21878174), and a grant from the Institute for Guo Qiang (2022GQS1001), Tsinghua University. The calculations were completed on the Shenzhen Bay Laboratory Computing Center and "Explorer 100" cluster system of Tsinghua HPC Platform.

## ■ REFERENCES


(1) Ge, J.; Lei, J.; Zare, R. N. Protein-inorganic hybrid nanoflowers. *Nat. Nanotechnol.* **2012**, *7*, 428−432.

(2) Panganiban, B.; Qiao, B.; Jiang, T.; DelRe, C.; Obadia, M. M.; Nguyen, T. D.; Smith, A. A. A.; Hall, A.; Sit, I.; Crosby, M. G.; Dennis, P. B.; Drockenmuller, E.; Olvera de la Cruz, M.; Xu, T. Random heteropolymers preserve protein function in foreign environments. *Science* **2018**, *359*, 1239−1243.

(3) DelRe, C.; Jiang, Y.; Kang, P.; Kwon, J.; Hall, A.; Jayapurna, I.; Ruan, Z.; Ma, L.; Zolkin, K.; Li, T.; Scown, C. D.; Ritchie, R. O.; Russell, T. P.; Xu, T. Near-complete depolymerization of polyesters with nano-dispersed enzymes. *Nature* **2021**, *592*, 558−563.

(4) Zhang, C.; Wu, W.; Li, R. Q.; Qiu, W. X.; Zhuang, Z. N.; Cheng, S. X.; Zhang, X. Z. Peptide-Based Multifunctional Nanomaterials for Tumor Imaging and Therapy. *Adv. Funct. Mater.* **2018**, *28*, 1804492.

(5) Howes, P. D.; Chandrawati, R.; Stevens, M. M. Colloidal nanoparticles as advanced biological sensors. *Science* **2014**, *346*, 1247390.

(6) Shin, T.-H.; Cheon, J. Synergism of Nanomaterials with Physical Stimuli for Biology and Medicine. *Acc. Chem. Res.* **2017**, *50*, 567−572.

(7) Sharifi, M.; Avadi, M. R.; Attar, F.; Dashtestani, F.; Ghorchian, H.; Rezayat, S. M.; Saboury, A. A.; Falahati, M. Cancer diagnosis using nanomaterials based electrochemical nanobiosensors. *Biosens. Bioelectron.* **2019**, *126*, 773−784.

(8) Nam, J.; Son, S.; Park, K. S.; Zou, W.; Shea, L. D.; Moon, J. J. Cancer nanomedicine for combination cancer immunotherapy. *Nat. Rev. Mater.* **2019**, *4*, 398−414.

(9) Nel, A. E.; Mädler, L.; Velegol, D.; Xia, T.; Hoek, E. M. V.; Somasundaran, P.; Klaessig, F.; Castranova, V.; Thompson, M. Understanding biophysicochemical interactions at the nano-bio interface. *Nat. Mater.* **2009**, *8*, 543−557.

(10) Lyu, F.; Zhang, Y.; Zare, R. N.; Ge, J.; Liu, Z. One-pot synthesis of protein-embedded metal-organic frameworks with enhanced biological activities. *Nano Lett.* **2014**, *14*, 5761.

(11) Ding, F.; Radic, S.; Chen, R.; Chen, P.; Geitner, N. K.; Brown, J. M.; Ke, P. C. Direct observation of a single nanoparticle-ubiquitin corona formation. *Nanoscale* **2013**, *5*, 9162−9169.

(12) Spanke, H. T.; Style, R. W.; François-Martin, C.; Feofilova, M.; Eisentraut, M.; Kress, H.; Agudo-Canalejo, J.; Dufresne, E. R. Wrapping of Microparticles by Floppy Lipid Vesicles. *Phys. Rev. Lett.* **2020**, *125*, 198102.

(13) Behzadi, S.; Serpooshan, V.; Tao, W.; Hamaly, M. A.; Alkawareek, M. Y.; Dreaden, E. C.; Brown, D.; Alkilany, A. M.; Farokhzad, O. C.; Mahmoudi, M. Cellular uptake of nanoparticles: journey inside the cell. *Chem. Soc. Rev.* **2017**, *46*, 4218−4244.

(14) Rawson, F. J.; Yeung, C. L.; Jackson, S. K.; Mendes, P. M. Tailoring 3D single-walled carbon nanotubes anchored to indium tin oxide for natural cellular uptake and intracellular sensing. *Nano Lett.* **2013**, *13*, 1−8.
(15) Pomastowski, P.; Sprynskyy, M.; Žuvela, P.; Rafińska, K.; Milanowski, M.; Liu, J. J.; Yi, M.; Buszewski, B. Silver-Lactoferrin Nanocomplexes as a Potent Antimicrobial Agent. *J. Am. Chem. Soc.* **2016**, *138*, 7899−7909.
(16) Li, X.; Cao, Y.; Luo, K.; Sun, Y.; Xiong, J.; Wang, L.; Liu, Z.; Li, J.; Ma, J.; Ge, J.; Xiao, H.; Zare, R. N. Highly active enzyme-metal nanohybrids synthesized in protein-polymer conjugates. *Nat. Catal.* **2019**, *2*, 718−725.
(17) Cao, Y.; Li, X.; Ge, J. Enzyme Catalyst Engineering toward the Integration of Biocatalysis and Chemocatalysis. *Trends Biotechnol.* **2021**, *39*, 1173−1183.
(18) Yang, J.; Wang, B.; You, Y.; Chang, W.-J.; Tang, K.; Wang, Y.-C.; Zhang, W.; Ding, F.; Gunasekaran, S. Probing the modulated formation of gold nanoparticles-beta-lactoglobulin corona complexes and their applications. *Nanoscale* **2017**, *9*, 17758−17769.
(19) Fu, J.; Yang, Y. R.; Johnson-Buck, A.; Liu, M.; Liu, Y.; Walter, N. G.; Woodbury, N. W.; Yan, H. Multi-enzyme complexes on DNA scaffolds capable of substrate channelling with an artificial swinging arm. *Nat. Nanotechnol.* **2014**, *9*, 531−536.
(20) Delebecque, C. J.; Lindner, A. B.; Silver, P. A.; Aldaye, F. A. Organization of intracellular reactions with rationally designed RNA assemblies. *Science* **2011**, *333*, 470−474.
(21) Dueber, J. E.; Wu, G. C.; Malmirchegini, G. R.; Moon, T. S.; Petzold, C. J.; Ullal, A. V.; Prather, K. L. J.; Keasling, J. D. Synthetic protein scaffolds provide modular control over metabolic flux. *Nat. Biotechnol.* **2009**, *27*, 753−759.
(22) Engström, K.; Johnston, E. V.; Verho, O.; Gustafson, K. P. J.; Shakeri, M.; Tai, C.-W.; Bäckvall, J.-E. Co-immobilization of an enzyme and a metal into the compartments of mesoporous silica for cooperative tandem catalysis: an artificial metalloenzyme. *Angew. Chem., Int. Ed.* **2013**, *52*, 14006−14010.
(23) Chen, Y.; Jiménez-Ángeles, F.; Qiao, B.; Krzyaniak, M. D.; Sha, F.; Kato, S.; Gong, X.; Buru, C. T.; Chen, Z.; Zhang, X.; Gianneschi, N. C.; Wasielewski, M. R.; Olvera de la Cruz, M.; Farha, O. K. Insights into the Enhanced Catalytic Activity of Cytochrome c When Encapsulated in a Metal-Organic Framework. *J. Am. Chem. Soc.* **2020**, *142*, 18576−18582.
(24) Weltz, J. S.; Kienle, D. F.; Schwartz, D. K.; Kaar, J. L. Reduced Enzyme Dynamics upon Multipoint Covalent Immobilization Leads to Stability-Activity Trade-off. *J. Am. Chem. Soc.* **2020**, *142*, 3463−3471.
(25) Filice, M.; Marciello, M.; Morales, M. d. P.; Palomo, J. M. Synthesis of heterogeneous enzyme-metal nanoparticle biohybrids in aqueous media and their applications in C-C bond formation and tandem catalysis. *Chem. Commun.* **2013**, *49*, 6876−6878.
(26) Chakraborty, I.; Feliu, N.; Roy, S.; Dawson, K.; Parak, W. J. Protein-Mediated Shape Control of Silver Nanoparticles. *Bioconjugate Chem.* **2018**, *29*, 1261−1265.
(27) Eby, D. M.; Schaeublin, N. M.; Farrington, K. E.; Hussain, S. M.; Johnson, G. R. Lysozyme catalyzes the formation of antimicrobial silver nanoparticles. *ACS Nano* **2009**, *3*, 984−994.
(28) Xiong, J.; Cai, X.; Ge, J. Enzyme−metal nanocomposites for antibacterial applications. *Particuology* **2021**, *64*, 134−139.
(29) Schneidman-Duhovny, D.; Inbar, Y.; Nussinov, R.; Wolfson, H. J. PatchDock and SymmDock: servers for rigid and symmetric docking. *Nucleic Acids Res.* **2005**, *33*, W363−W367.
(30) Pastore, C. Size-dependent nano-bio interactions. *Nat. Nanotechnol.* **2021**, *16*, 1052.
(31) Albanese, A.; Tang, P. S.; Chan, W. C. W. The effect of nanoparticle size, shape, and surface chemistry on biological systems. *Annu. Rev. Biomed. Eng.* **2012**, *14*, 1−16.
(32) Wang, Y.; Cai, R.; Chen, C. The Nano−Bio Interactions of Nanomedicines: Understanding the Biochemical Driving Forces and Redox Reactions. *Acc. Chem. Res.* **2019**, *52*, 1507−1518.
(33) Agarwal, P. K.; Schultz, C.; Kalivretenos, A.; Ghosh, B.; Broedel, S. E. Engineering a Hyper-catalytic Enzyme by Photoactivated Conformation Modulation. *J. Phys. Chem. Lett.* **2012**, *3*, 1142−1146.
(34) Luo, J.; Bruice, T. C. Ten-nanosecond molecular dynamics simulation of the motions of the horse liver alcohol dehydrogenase.PhCH2O- complex. *Proc. Natl. Acad. Sci. U.S.A.* **2002**, *99*, 16597−16600.
(35) Rodriguez-Bussey, I.; Yao, X.-Q.; Shouaib, A. D.; Lopez, J.; Hamelberg, D. Decoding Allosteric Communication Pathways in Cyclophilin A with a Comparative Analysis of Perturbed Conformational Ensembles. *J. Phys. Chem. B* **2018**, *122*, 6528−6535.
(36) Yao, X.-Q.; Hamelberg, D. Detecting Functional Dynamics in Proteins with Comparative Perturbed-Ensembles Analysis. *Acc. Chem. Res.* **2019**, *52*, 3455−3464.
(37) Wheeldon, I.; Minteer, S. D.; Banta, S.; Barton, S. C.; Atanassov, P.; Sigman, M. Substrate channelling as an approach to cascade reactions. *Nat. Chem.* **2016**, *8*, 299−309.
(38) Liu, Y.; Hickey, D. P.; Guo, J.-Y.; Earl, E.; Abdellaoui, S.; Milton, R. D.; Sigman, M. S.; Minteer, S. D.; Calabrese Barton, S. Substrate Channeling in an Artificial Metabolon: A Molecular Dynamics Blueprint for an Experimental Peptide Bridge. *ACS Catal.* **2017**, *7*, 2486−2493.
(39) Uppenberg, J.; Hansen, M. T.; Patkar, S.; Jones, T. A. The sequence, crystal structure determination and refinement of two crystal forms of lipase B from Candida antarctica. *Structure* **1994**, *2*, 293−308.
(40) Søndergaard, C. R.; Olsson, M. H.; Rostkowski, M.; Jensen, J. H. Improved Treatment of Ligands and Coupling Effects in Empirical Calculation and Rationalization of pKa Values. *J. Chem. Theory Comput.* **2011**, *7*, 2284.
(41) Olsson, M. H. M.; Søndergaard, C. R.; Rostkowski, M.; Jensen, J. H. PROPKA3: Consistent Treatment of Internal and Surface Residues in Empirical pKa Predictions. *J. Chem. Theory Comput.* **2011**, *7*, 525−537.
(42) Woods Group *GLYCAM Web*; Complex Carbohydrate Research Center, University of Georgia: Athens, GA, 2005−2021 (http://glycam.org).
(43) Hess, B.; Kutzner, C.; van der Spoel, D.; Lindahl, E. GROMACS 4: Algorithms for Highly Efficient, Load-Balanced, and Scalable Molecular Simulation. *J. Chem. Theory Comput.* **2008**, *4*, 435−447.
(44) Hornak, V.; Abel, R.; Okur, A.; Strockbine, B.; Roitberg, A.; Simmerling, C. Comparison of multiple Amber force fields and development of improved protein backbone parameters. *Proteins* **2006**, *65*, 712−725.
(45) Doshi, U.; Hamelberg, D. Reoptimization of the AMBER Force Field Parameters for Peptide Bond (Omega) Torsions Using Accelerated Molecular Dynamics. *J. Phys. Chem. B* **2009**, *113*, 16590−16595.
(46) Kirschner, K. N.; Yongye, A. B.; Tschampel, S. M.; González-Outeiriño, J.; Daniels, C. R.; Foley, B. L.; Woods, R. J. GLYCAM06: A generalizable biomolecular force field. Carbohydrates. *J. Comput. Chem.* **2008**, *29*, 622−655.
(47) Daw, M. S.; Foiles, S. M.; Baskes, M. I. The Embedded-Atom Method - a Review of Theory and Applications. *Mater. Sci. Rep.* **1993**, *9*, 251−310.
(48) Heinz, H.; Lin, T.-J.; Kishore Mishra, R.; Emami, F. S. Thermodynamically consistent force fields for the assembly of inorganic, organic, and biological nanostructures: the INTERFACE force field. *Langmuir* **2013**, *29*, 1754−1765.
(49) Heinz, H.; Vaia, R. A.; Farmer, B. L.; Naik, R. R. Accurate Simulation of Surfaces and Interfaces of Face-Centered Cubic Metals Using 12-6 and 9-6 Lennard-Jones Potentials. *J. Phys. Chem. C* **2008**, *112*, 17281−17290.
(50) Coppage, R.; Slocik, J. M.; Ramezani-Dakhel, H.; Bedford, N. M.; Heinz, H.; Naik, R. R.; Knecht, M. R. Exploiting localized surface binding effects to enhance the catalytic reactivity of peptide-capped nanoparticles. *J. Am. Chem. Soc.* **2013**, *135*, 11048−11054.


https://doi.org/10.1021/jacsau.2c00077
*JACS Au* 2022, 2, 961−971

(51) Kumari, R.; Kumar, R.; Lynn, A. g_mmpbsa–a GROMACS tool for high-throughput MM-PBSA calculations. *J. Chem. Inf. Model.* **2014**, *54*, 1951−1962.
(52) Valdes-Tresanco, M. S.; Valdes-Tresanco, M. E.; Valiente, P. A.; Moreno, E. gmx_MMPBSA: A New Tool to Perform End-State Free Energy Calculations with GROMACS. *J. Chem. Theory Comput.* **2021**, *17*, 6281−6291.
(53) Miller, B. R., 3rd; McGee, T. D., Jr.; Swails, J. M.; Homeyer, N.; Gohlke, H.; Roitberg, A. E. MMPBSA.py: An Efficient Program for End-State Free Energy Calculations. *J. Chem. Theory Comput.* **2012**, *8*, 3314−3321.
(54) Bussi, G.; Donadio, D.; Parrinello, M. Canonical sampling through velocity rescaling. *J. Chem. Phys.* **2007**, *126*, 014101.
(55) Parrinello, M.; Rahman, A. Crystal Structure and Pair Potentials: A Molecular-Dynamics Study. *Phys. Rev. Lett.* **1980**, *45*, 1196−1199.
(56) Hess, B.; Bekker, H.; Berendsen, H. J. C.; Fraaije, J. G. E. M. LINCS: A linear constraint solver for molecular simulations. *J. Comput. Chem.* **1997**, *18*, 1463−1472.
(57) Case, D.; Ben-Shalom, I.; Brozell, S.; Cerutti, D.; Cheatham, T.; Cruzeiro, V.; Darden, T.; Duke, R.; Ghoreishi, D.; Gilson, M. *AMBER 18*; University of California: San Francisco, 2018.
(58) Wang, J.; Wolf, R. M.; Caldwell, J. W.; Kollman, P. A.; Case, D. A. Development and testing of a general amber force field. *J. Comput. Chem.* **2004**, *25*, 1157−1174.
(59) Bayly, C. I.; Cieplak, P.; Cornell, W.; Kollman, P. A. A well-behaved electrostatic potential based method using charge restraints for deriving atomic charges: the RESP model. *J. Phys. Chem. A* **2002**, *97*, 10269−10280.
(60) Case, D.; Ben-Shalom, I.; Brozell, S.; Cerutti, D.; Cheatham, T.; Cruzeiro, V.; Darden, T.; Duke, R.; Ghoreishi, D.; Giambasu, G. *Amber 2019*; University of California: San Francisco, 2019.
(61) Humphrey, W.; Dalke, A.; Schulten, K. VMD: visual molecular dynamics. *J. Mol. Graph.* **1996**, *14*, 33.
(62) Martinez, L. Automatic identification of mobile and rigid substructures in molecular dynamics simulations and fractional structural fluctuation analysis. *PLoS One* **2015**, *10*, No. e0119264.
(63) Grant, B. J.; Rodrigues, A. P.; ElSawy, K. M.; McCammon, J. A.; Caves, L. S. Bio3d: an R package for the comparative analysis of protein structures. *Bioinformatics* **2006**, *22*, 2695−2696.
(64) Shkurti, A.; Goni, R.; Andrio, P.; Breitmoser, E.; Bethune, I.; Orozco, M.; Laughton, C. A. pyPcazip: A PCA-based toolkit for compression and analysis of molecular simulation data. *SoftwareX* **2016**, *5*, 44−50.
(65) McGibbon, R. T.; Beauchamp, K. A.; Harrigan, M. P.; Klein, C.; Swails, J. M.; Hernandez, C. X.; Schwantes, C. R.; Wang, L. P.; Lane, T. J.; Pande, V. S. MDTraj: A Modern Open Library for the Analysis of Molecular Dynamics Trajectories. *Biophys. J.* **2015**, *109*, 1528−1532.


https://doi.org/10.1021/jacsau.2c00077
*JACS Au* 2022, 2, 961−971